THE JOURNAL OF PHYSICAL CHEMISTRY C

Article

pubs.acs.org/JPCC

Fast-Scan Cyclic Voltammetry Allows Determination of Electron-Transfer Kinetic Constants in Single Nanoparticle Collision

Stephen J. Percival and Bo Zhang*

Department of Chemistry, University of Washington, Seattle, Washington 98195-1700, United States

Supporting Information

ABSTRACT: Here we report the use of Fast-Scan Cyclic Voltammetry (FSCV) to study transient nanoparticle (NP) collision experiments and determine the apparent heterogeneous electron-transfer (ET) rate constant k^o and electrocatalytic activity of single NPs. Continuous potential scanning at fast scan rates, for example, up to 500 V/s, and background subtraction enable voltammetric study of single NPs when they collide on a carbon ultramicroelectrode (UME). The FSCV results indicate a substantial potential shift in the CV response of single NPs due to increased mass transfer and it is necessary to consider this effect when analyzing single NP electrocatalysts. FSCV results also reveal that single particle deactivation is associated with a decrease in peak current and an increase in overpotential. Importantly, the use of FSCV coupled with numerical simulations enabled the determination of k^o on single NPs, confirming an increase in catalytic activity with decreasing particle size. Moreover, the Gibbs free energy of activation can be estimated from the k^o. This work further confirms that FSCV is a powerful method in studying dynamic electrochemical processes such as single NP collisions.

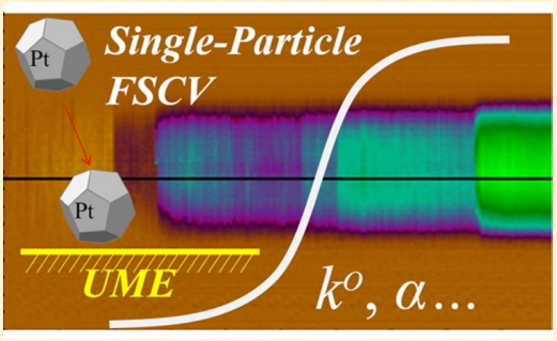

INTRODUCTION

The ability to observe and study single, transient electrochemical events offers tremendous opportunity in developing a deeper understanding of electron-transfer processes at the electrode/solution interface as well as in other areas, such as electrocatalysis and highly sensitive sensors. A direct study of single redox molecules has been particularly challenging due to the extremely low charge signal (order of 10^{-19} C) and high electrical noise. However, single molecules can be studied by carefully designing electrode geometry and utilizing redox cycling in a nanometer-scale gap between two electrodes.[1−3] Single nanoparticles (NPs), on the other hand, can be more readily studied with the use of an ultramicroelectrode (UME). Single-NP electrochemistry has quickly gained much attention in the past decade.

Metal NPs are key materials in electrochemistry and many other fields, such as biotechnology,[4,5] sensing,[6,7] and catalysis.[8−10] Their electrocatalytic activity is often strongly dependent on size,[9,11−13] shape,[10,14,15] capping agents,[16] and composition.[8,17] As such, single NP electrochemistry could be especially useful for better understanding structure−function relationship in NP electrocatalysis.

Several single-NP methods have been reported in literature, which all involve the use of an UME to record transient electrochemical events. Lemay and co-workers reported one of the earliest attempts in which they recorded transient blocking events of single insulating NPs on an UME.[18] The attachment of an insulating NP on an UME reduces the total flux of redox molecules resulting in an individual current decay step. Crooks group has used optical microscopy and numerical simulation in conjunction with amperometry to develop a detailed understanding of current blockage and particle attachment, motion, and aggregation on the electrode surface.[19] Bard and co-workers have demonstrated the detection of single viruses[20] and emulsion nanodroplets.[21]

The second method uses an electrocatalytically inactive UME, such as carbon fiber, to measure catalytic current response of single collision events as NPs collide on the UME and "turn on" an inner-sphere redox reaction, such as proton reduction, on the electrode.[22−25] Figure 1A shows a scheme of a collision experiment where a small constant overpotential is applied on a detector UME under which there is little or no oxidation of hydrazine on the electrode (*situation I*). However, when a metal NP collides and sticks to the electrode surface, a current increase is immediately detected due to the catalytic enhancement on the NP (*situation II*). This method has received considerable interest in the past few years and a number of exciting advancements have been reported by Bard and several other groups. Stevenson's group has reported the use of Hg-modified UMEs, which drastically reduces electrical noise and baseline shift during recording and increases reproducibility. A fresh electrode surface is maintained due to quick deactivation of NPs on Hg.[26] Unwin and co-workers have

Special Issue: Richard P. Van Duyne Festschrift

Received: November 19, 2015
Revised: March 28, 2016
Published: March 29, 2016

DOI: 10.1021/acs.jpcc.5b11330
J. Phys. Chem. C 2016, 120, 20536−20546

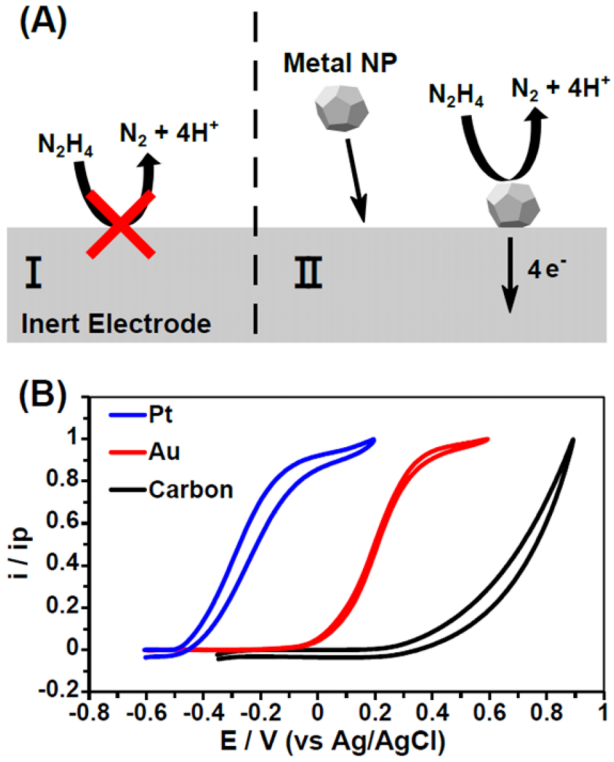

Figure 1. (A) Schematic illustration showing the generalized process of a NP collision experiment where in situation (I) hydrazine oxidation is kinetically unfavorable on the UME itself and in situation (II) hydrazine oxidation takes place on a NP when it collides with the UME. (B) A graph of normalized CVs of hydrazine oxidation on three different electrode materials where the catalytic activity of these materials determines the oxidation potential. All CVs were taken at 50 mV/s in an aqueous solution containing 10 mM hydrazine and 50 mM phosphate buffer (pH 7.4).

begun to elucidate some of the complex interactions between the NP and the electrode using ultrafast recording.[27] Stevenson and Crooks have examined the role of increased mass transfer on the frequency and magnitude of current steps in microfluidic devices.[28] Kwon and co-workers have made new insights into the effect of the applied voltage on the shape of the current steps.[29] Alpuche-Aviles's group has reported an interesting study to examine the photoelectrochemical response of individual NPs during collision.[30] Some of the most recent work includes the observation of transient catalytic signal of single enzymes[31] and the study of electrocatalytic reduction of AgCl on single metal NPs.[32]

Single NP collisions can also be observed when they are directly oxidized or reduced on the UME. Compton's group first reported the electrochemical oxidation and dissolution of single silver NPs and reduction of fullerene NPs.[33,34] Alpuche-Aviles's group reported the detection of single ZnO NPs on an Hg UME.[35] In addition to metal and metal oxide, this concept is also well suited for the study of transient events on redox-containing emulsions[21] and vesicles.[36]

The electrochemistry of single NPs can also be studied when NPs are isolated and immobilized on a small electrode. A number of techniques have been used for this purpose ranging from surface plasmon resonance,[37] single-molecule florescence[38,39] and direct electrical characterization using nanoelectrodes,[40−43] to scanning electrochemical microscopy (SECM).[44] It is important to note that it can be quite challenging to isolate and immobilize individual nanoparticles on electrode surfaces. Compared to single particle immobilization, collision-based transient NP electrochemistry is a powerful means for studying hundreds or even thousands of particles in minutes.

Our group has recently reported the use of FSCV (developed by Millar[45] and popularized by Wightman[46,47]) to examine single NP collisions. A unique aspect of FSCV method is that one can record voltammetry responses of individual NPs and this enables collection of chemical information unobtainable in many constant-potential experiments.[48] In this work we extend our ability and demonstrate the use of FSCV in the study of single NP electron-transfer (ET) kinetics and electrocatalytic activity of single NP. The use of FSCV allows us to discuss nanoparticle size effects on ET kinetics and electrocatalytic activity. We also illustrate a strong mass-transfer effect at small NPs, which shifts the oxidation wave to higher overpotentials as NP size decreases. This overpotential shift can erroneously make smaller particles appear less catalytically active. The use of single NP CV data, when combined with theory or numerical simulations that account for the increased mass-transfer, enables us to extract useful catalytic information on individual NPs. We specifically focus on ET kinetic parameters, such as the standard rate constant, k^o, and the charge transfer coefficient, α, for hydrazine oxidation on gold and platinum NPs from 4 to 50 nm. Furthermore, NP deactivation was examined for the first time using FSCV. Finally, the Gibbs free energy of activation, $\Delta G^{\ddagger}$, for different NPs was also calculated from their k^o and is found to be smaller than bulk metals and decreases with decreasing NP size.

RESULTS AND DISCUSSION

Electrocatalytic Oxidation of Hydrazine on Single NPs. Hydrazine oxidation is of great interest to fuel cell applications but the reaction occurs at high overpotentials even on active catalysts.[49] The overall reaction in a basic solution is a four-electron process,[50]

$$N_2H_4 + 4OH^- \rightarrow N_2 + 4H_2O + 4e^- \quad (1)$$

The standard potential, E^o, is −0.33 V versus RHE[50] or −0.56 V versus Ag/AgCl. In Figure 1A, the use of carbon as the UME ensures the amount of oxidation current collected on the working electrode is minimized. The electrocatalytic activity of different electrode materials are compared in Figure 1B, and the results clearly show platinum is the most active material followed by gold and carbon. Carbon, in fact, does not attain the diffusion limited current at these potential ranges and at 0.5 V (a potential beyond where Au has already attained the diffusion limited steady state current) the current on the 5 um diameter carbon electrode is ∼1.1 nA (56.9 pA/um^2 current density) and is only 2% of the expected limiting current.

Three sizes of NPs are employed in this study for both gold and platinum (six types in total). The NP sizes were determined with TEM and the reported diameter is the average size. Citrate capped gold NPs were 5, 12, and 50 nm in diameter. The Pt NPs included 4 and 30 nm citrate capped spherical NPs and 10 nm polyacrylate capped cubic particles.

In FSCV, a repetition rate in the range of 10−100 Hz generates hundreds to thousands of CVs in a typical 60-s period. Depending on the collision frequency, one can obtain several tens of CVs on each NP following its collision with the UME and prior to collision of another particle. The frequency of collision events is typically much lower than expected,

DOI: 10.1021/acs.jpcc.5b11330
J. Phys. Chem. C 2016, 120, 20536−20546

possibly due to the formation of NP aggregates in hydrazine solution,[51] effectively lowering the concentration allowing sufficient time between NP collisions to collect many CVs from each event. A color plot enables quick examination of dynamic redox events.[52] Figure 2A shows five collision events

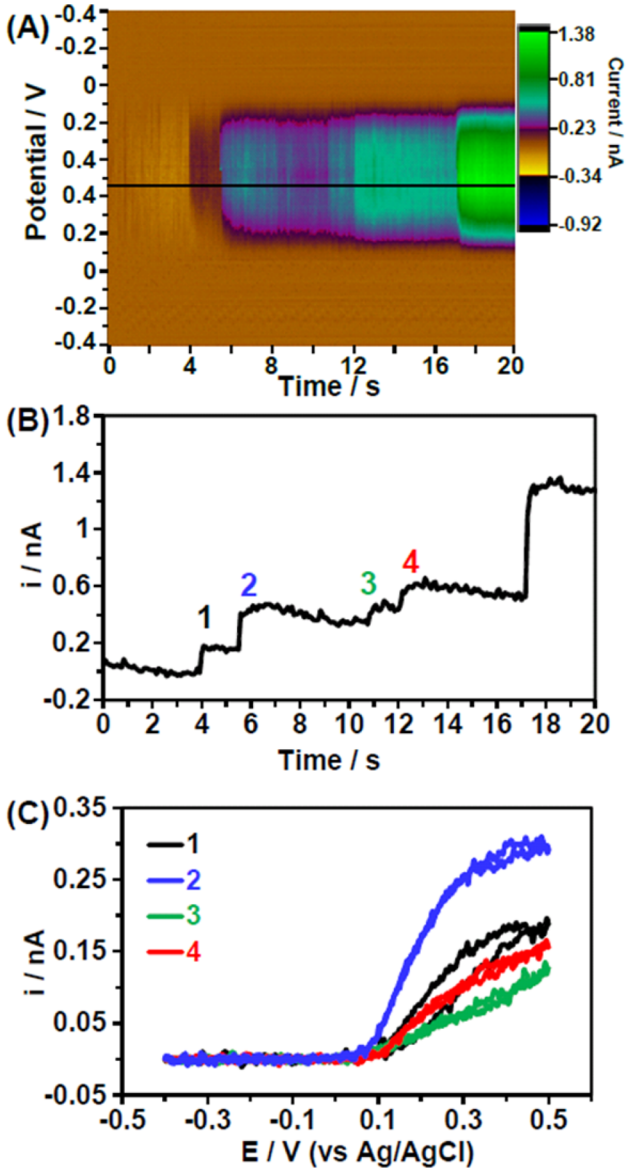

Figure 2. (A) Typical FSCV color plot showing the detection of 12 nm Au NPs on a carbon UME. (B) Current vs time trace taken from the color plot in (A) at 0.465 V in the forward scan (along the black line). (C) Background-subtracted, single-particle CVs from the events marked in (B). The solution contains 10 mM hydrazine, 50 mM phosphate buffer (pH 7.4), and ~12.5 pM Au NPs (12 nm), cycled at 25 V/s scan rate.

on a 60 s recording of 12 nm Au NPs in 10 mM hydrazine where the current increases in a stair step manner due to hydrazine oxidation on gold NPs. The current increases can also be visualized by directly plotting the $i-t$ trace at a selected potential. Figure 2B is an $i-t$ trace at 0.465 V indicated by the black line in the color plot. Four of the five collision events were labeled and their representative CVs plotted in Figure 2C. Events 1, 2, and 4 have characteristic sigmoidal shape CVs, indicating they are diffusion (mass transport) limited. Event 3 does not reach the diffusion limitation in this potential range and thus hydrazine oxidation is likely still under kinetic control. Further increasing the potential would cause event 3 to reach a diffusion-limited state. However, this would lead to a large background current on the carbon UME. The fifth event at ~17 s (unlabeled in the plots) has a large current step indicating it is due to a particle aggregate.[51] Only events that were observed to reach the diffusion limited steady state current with i_{ss} current below a threshold current (the predicted current of a particle that has a radius within three standard deviations from the average TEM determined NP radius) were kept, that is, aggregates and kinetically limited events were discarded. The limiting current is estimated using the equation for a spherical particle on a planar surface,[23]

$$i_{ss} = 4\ln(2)\pi nFDC^{*}r \quad (2)$$

where n is the number of electrons transferred per molecule ($n = 4$), F is the Faraday constant, $D = 1.39 \times 10^{-5}$ cm^2/s is the diffusion coefficient,[53] C^* is the bulk concentration, and r is the particle radius. This equation was also used to determine the size of the NPs from the sample events that were simulated, discussed in detail below.

Single NP CVs were analyzed by first plotting the half-wave potential, $E_{1/2}$, and the onset potential, E_{onset} (defined as the potential when the current reaches 20% of the i_{ss}) versus the diffusion limited current for each collision event, presented in Figure 3. Figure 3A and B are scatter plots for gold NPs and Figure 3C and D are for platinum. A closer inspection of these results reveals several distinct features in the distributions of the scattered points. First, the Pt NPs display higher catalytic activities than the gold with more negative E_{onset} and $E_{1/2}$ potentials. Second, smaller Pt NPs are found to group around a more positive potential, whereas the larger ones are spread out more.

Interestingly, the 30 nm Pt NPs show catalytic activity that is much more scattered than the other sizes. This is significantly distinct from the 50 nm Au particles which display more uniform catalytic activities possibly due to the high degree of polycrystallinity in the 30 nm Pt NPs. Furthermore, the E_{onset} plots show narrower distributions than the $E_{1/2}$ plots. This is more apparent when the events are plotted in histograms, shown in Figure S4, where there is a higher probability of a particle displaying a given E_{onset} within the smaller range than for the $E_{1/2}$. This can be observed for all the NP batches but is most prominent for the 12 and 50 nm diameter gold NPs.

By averaging the responses from all of the single NP events and plotting them versus $1/r$ (average TEM radius) a clearer trend emerges. The oxidation potentials on Au NPs form a linear trend with the $1/r$, as seen in Figure 4A,B. All of the tested Au and Pt NPs have more positive $E_{1/2}$ and E_{onset} than their corresponding bulk metals. The E_{onset} and $E_{1/2}$ were measured at 107 and 204 mV versus Ag/AgCl for bulk gold, which are very close to the most active 50 nm gold NPs. The bulk gold values were negatively shifted by approximately 23 mV (E_{onset}) and 7 mV ($E_{1/2}$) than the 50 nm Au NPs. On the other hand, the E_{onset} and $E_{1/2}$ for bulk Pt were −244 and −349 mV versus Ag/AgCl, respectively, which are much further from the most active Pt NPs, in stark contrast to the gold NPs. The bulk Pt was shifted by approximately 253 mV (E_{onset}) and 324 mV ($E_{1/2}$) more negative than the 30 nm Pt NPs, which are also plotted versus the inverse of the radius in Figure 4C,D. In these plots we again see that the smaller 4 nm Pt NPs are

DOI: 10.1021/acs.jpcc.5b11330
J. Phys. Chem. C 2016, 120, 20536−20546

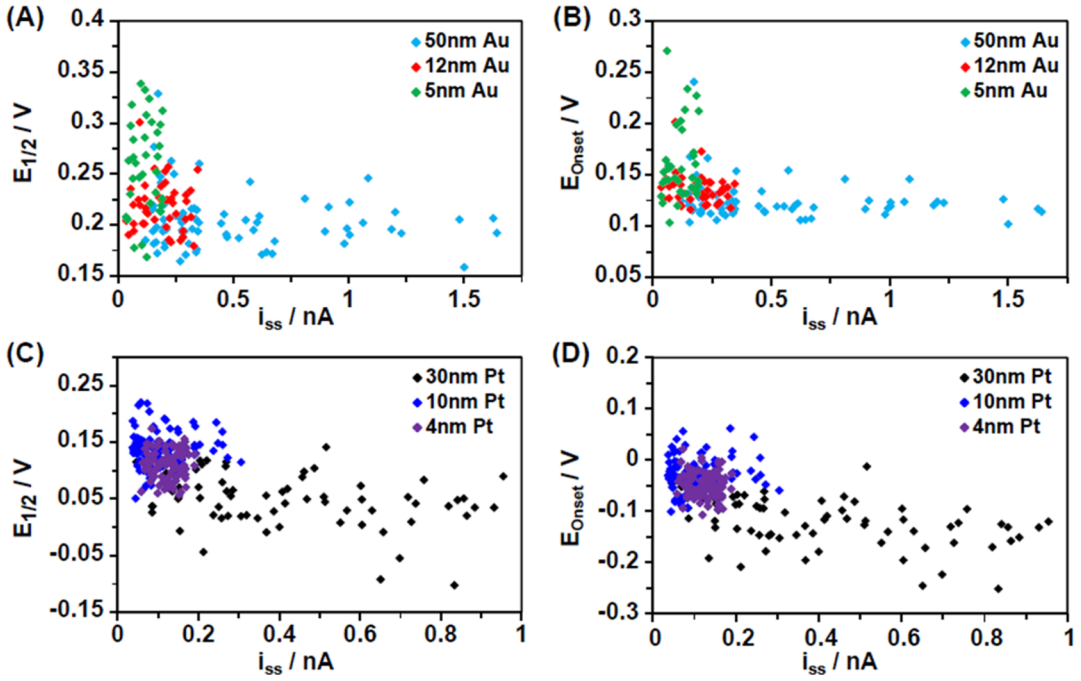

Figure 3. Scatter plots showing the $E_{1/2}$ and E_{onset} (potential at 20% of i_{ss}) vs the mass transfer limited steady state current for gold NPs (A) and (B) and platinum NPs (C) and (D). The points plotted for the E_{onset} are from the same events seen in the $E_{1/2}$ plots and all are plotted in reference to Ag/AgCl. The number of events plotted for each particle size are listed in Table S3 in the Supporting Information.

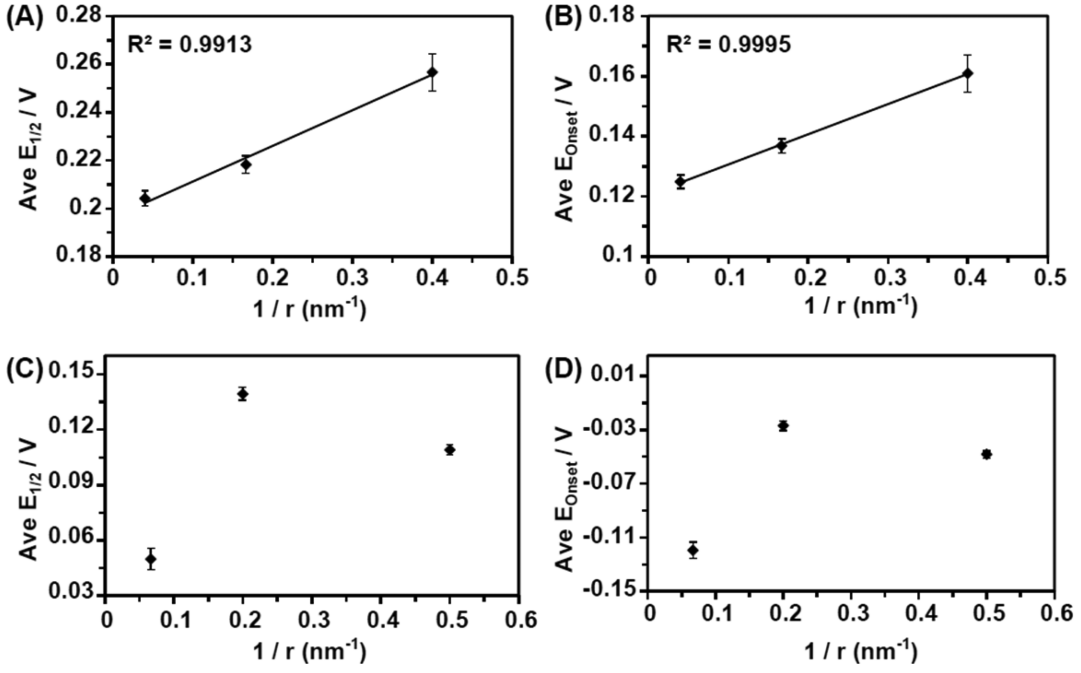

Figure 4. Plots of the averaged $E_{1/2}$ and E_{onset} from all the mass transfer limited steady state CV NP events seen in the scatter plot, averaged for each NP colloidal solution and plotted as the inverse of the TEM determined radius. (A) and (B) are from the gold NPs and (C) and (D) are from the platinum NPs. Error bars indicate standard error of the mean.

shifted to more positive potentials as compared to the larger 30 nm Pt NPs.

We note that the normal procedure of using E_{onset} and $E_{1/2}$ to discuss catalytic activity of NPs,[54,55] should be carefully evaluated for single-particle studies. Despite well documented evidence from many studies that smaller NPs are more active catalysts,[56] the opposite trend can be observed when only the $E_{1/2}$ and E_{onset} potentials are examined. We would like to state again that we are not trying to refute the many reported cases where the catalytic activity increases for smaller particles, but that great care needs to be taken when examining activities of single isolated nanoparticles and that simply looking at $E_{1/2}$ and E_{onset} potentials is not sufficient to determine the activities.

We believe this effect is largely due to an increased mass transfer rate at nanoscale electrodes, which has been observed before.[57,58] The mass transfer coefficient, $m_o = D/r$, at an

DOI: 10.1021/acs.jpcc.5b11330
J. Phys. Chem. C 2016, 120, 20536−20546

ultramicroelectrode[42,59] (or nanoparticle) increases as the electrode gets smaller. Compared to NP ensembles, the use of single NPs eliminates effects of overlapping diffusion layers.[60] The observed overpotential shift is due to the increased reaction rate that is necessary in order to compensate for the increased rate of reactant transport (mass transfer) to smaller particles. To achieve the increased rate of the anodic reaction, the potential must be increased in accordance with eq 5, discussed in more detail below, where increasing the potential will lead to an ever increasing value for the anodic rate constant, k_a (i.e., forward reaction rate), which must be increased until it matches the mass transfer rate.

However, we first believed that there could have been a substrate effect causing the positive potential shift in single particle collision. Such effect is especially strong with Pt NPs where the substrate can either enhance or inhibit NP activity.[61] Additionally, the capping ligands could have been interfering with the activity more strongly on smaller NPs. While these effects may have a subtle effect, we believe the increased mass transport is the dominating influence. To further test this hypothesis, we conducted hydrazine oxidation on bare Pt nanoelectrodes that are free of ligand or substrate effects and the results in Figure S5 show a clear positive shift similar to the NPs. The observed increased mass transport effects on small NPs have implications for single particle studies. When discussing single NP electrocatalysis, simply comparing the E_{onset} or $E_{1/2}$ may lead to a misinterpretation of the results. Single-particle CVs on different-sized NPs must be combined with kinetic analysis in order to extract useful electrocatalytic information.

A comparison of E_{onset} and $E_{1/2}$ between the 4 and 10 nm Pt NPs has revealed another possible ligand or crystal defect density effect. Despite a predicted positive potential shift on the 4 nm Pt NPs due to the increased mass transfer coefficient, Figure 4C,D have shown a clear positive shift on the 10 nm Pt particles. The shift may be attributed to the presence of the larger polyacrylate capping ligands and a stronger blocking effect compared to the citrate molecules. Polyacrylate may also change the electron density of these particles in a different manner than citrate.[62] The 10 nm particles are mostly single crystalline cubic particles, possessing {100} crystal faces, which are known to have higher activities for hydrazine oxidation, shown in experiments with single crystal platinum electrodes,[63] than the more abundant {111} crystal faces on typical citrate capped Pt NPs.[64] However, recent experiments have shown the opposite trend where hydrazine oxidation is found to be better on high index, high defect crystal faces,[65] which the 4 and 30 nm particles most likely have a very high density of defects and grain boundaries that could contribute to the activity.

Voltammetric Insights into Nanoparticle Deactivation. Some particles are often seen to display a decrease in the peak current over time after their initial collision. This "deactivation" process has been observed in previously studies[22−24] with little or no voltammetric insight. The changing activity over time, if any, of a deactivating particle can be examined using FSCV to monitor its deactivation process. An example of this can be seen in Figure 5A, which shows an i−t trace taken from a FSCV scan. A platinum NP is detected giving the characteristic stepped current increase, but the current decreases over time. Figure 5B shows a number of extracted CVs (forward scan only) taken from the red points in (A) which are seen to be kinetically limited. The CVs display gradual decrease in peak current and an apparent shift to more positive potentials with time. The potentials to reach 0.4 and 0.2 nA plotted in Figure 5C shift positively as it deactivates over time. This indicates that both the current and the catalytic activity decrease during NP deactivation. This observation is very interesting because potential cycling is typically used to activate a catalyst surface,[66] and this nanoparticle is being cycled at a fast rate but is still observed to deactivate. This deactivation may be due to gradual dissolution of the particle, gradual poisoning of the platinum surface or conversion of part of the particle surface to a less reactive material skin such as a fast growing, thick insulating layer of platinum oxide.[67] However, we are unsure of what causes this deactivation process at this time as hydrazine oxidation is a very complicated

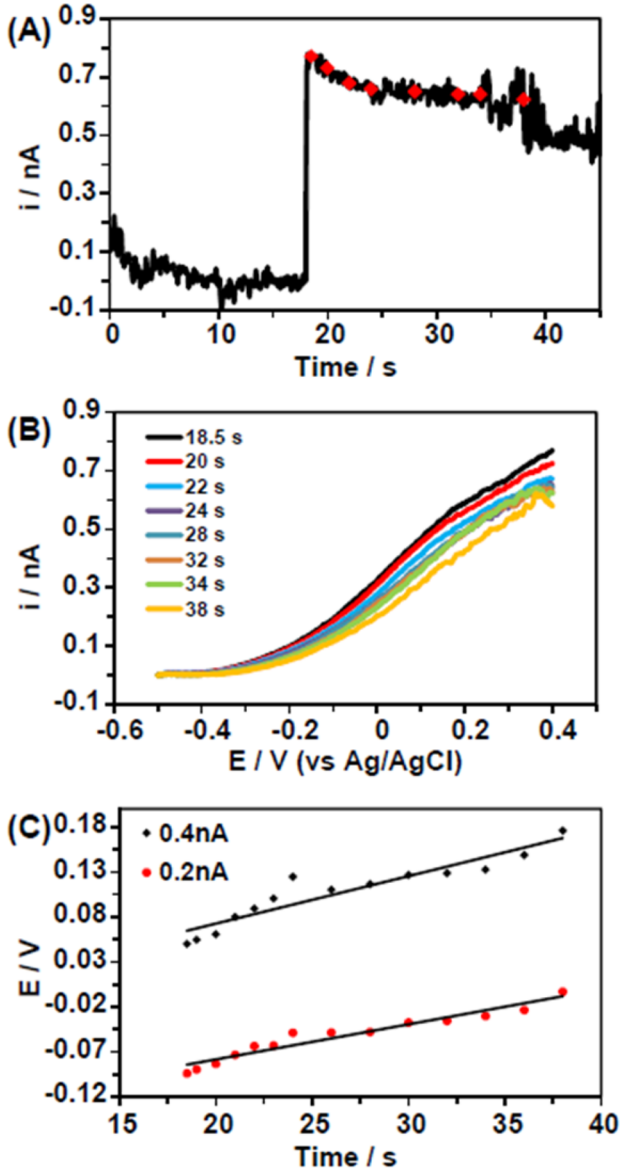

Figure 5. (A) Current−time trace showing a collision event of a platinum NP where the particle is seen to deactivate, indicated by the decrease in peak current. (B) Example CVs (forward scan only) taken from the FSCV scan at the points indicated by the red dots in (A). (C) Positive shifting of the potential to reach current magnitudes of 0.2 nA and 0.4 nA as the particle deactivates. The current−time trace was taken from the FSCV scan at the point where the potential was 0.4 V; Cycled at 25 V/s scan rate, 10 mM hydrazine, and 50 mM phosphate buffer.

DOI: 10.1021/acs.jpcc.5b11330
J. Phys. Chem. C 2016, 120, 20536−20546

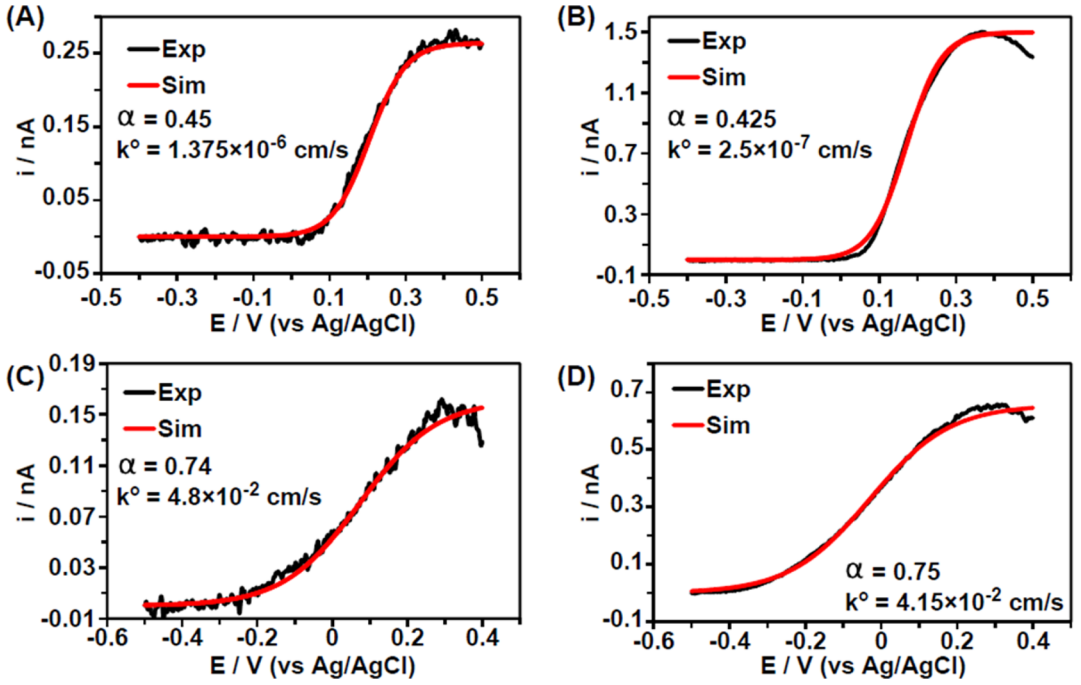

Figure 6. Experimental CV curves and their corresponding simulation from four example NPs from the listed colloidal solutions: (A) 12 nm Au, (B) 50 nm Au, (C) 4 nm Pt, and (D) 30 nm Pt. Simulated CVs were obtained using the listed parameters. Only the forward scans are shown, and each experimental CV was taken at 25 V/s in 10 mM hydrazine containing 50 mM phosphate buffer (pH 7.4). Actual calculated diameter of the NPs used in these example simulations are (A) 11.43 nm Au, (B) 64.23 nm Au, (C) 6.94 nm Pt, and (D) 28.14 nm Pt.

reaction and there are conflicting reports about the role platinum surface oxides play in hydrazine oxidation,[65,66] but it is something that we will investigate further.

Electron-Transfer Kinetics at Single Nanoparticles. The use of FSCV allows us to extract useful kinetic information from single NPs. Here, single NP CVs are simulated with a finite-element simulation program, Comsol, by incorporating Butler–Volmer kinetics. We first considered a typical redox couple where an oxidized species O are reduced to R by an $n-e^-$ process as following,

$$O + ne^- \underset{k_a}{\overset{k_c}{\leftrightarrow}} R \tag{3}$$

with k_c and k_a being the cathodic and anodic rate constants, respectively. These rates can be expressed according to Butler–Volmer kinetics as

$$k_c = k^\circ \exp\left[-\alpha\left(\frac{nF}{RT}\right)(E_{app} - E^\circ)\right] \tag{4}$$

$$k_a = k^\circ \exp\left[(1-\alpha)\left(\frac{nF}{RT}\right)(E_{app} - E^\circ)\right] \tag{5}$$

where k° is the standard electron transfer rate constant, α is the charge transfer coefficient, and E_{app} is the applied potential. All other parameters have been previously given. The oxidation of adsorbed hydrazine is a totally irreversible reaction having a $1-e^-$ rate-determining step (RDS) as the initial oxidation step followed by the remaining three very fast $1-e^-$ oxidation steps,[49,68,69]

$$N_2H_4(ads) \xrightarrow{RDS} N_2H_3(ads) + H^+ + 1e^- \tag{6}$$

$$N_2H_3(ads) \xrightarrow{FAST} N_2 + 3H^+ + 3e^- \tag{7}$$

For a totally irreversible reaction of this type, where the initial step is rate determining, the overall result is given by the forward rate constant, k_a.[70] The flux of the diffusing hydrazine to the NP surface can then be expressed as

$$j = -k^\circ \exp\left[(1-\alpha)\left(\frac{F}{RT}\right)(E_{app} - E^\circ)\right] \times C_R \tag{8}$$

where C_R is the hydrazine concentration at the electrode surface. The values of both α and k° were varied in the simulation until the simulated CV closely matched the experiment. A spherical geometry was assumed for the NPs in the simulation and a discussion of the simulation environment and effect that changing α or k° has on the simulated CV can be found in the Supporting Information.

Figure 6 shows four experimental and simulated CVs and the parameters used in the simulation. Figure 6A and B are for the 12 and 50 nm Au NPs and 6C and D are for the 4 and 30 nm Pt NPs, respectively. The simulation overall matches well with the experiments, but for the larger NPs, the simulation begins to deviate slightly from the experimental curve. Some possible reasons are the mismatch in particle shapes (compared to the simulation), the presence of well-defined crystal faces and NP surface roughness. The simulation assumed spherical particles, whereas the TEM reveals that they can diverge from spherical geometry, especially for the larger particles. The 30 nm Pt NPs appear rough and the 50 nm Au NPs can be more oblong. The presence of specific crystal faces and surface roughness may lead to preadsorption of the reactant[49,63] on some faces that is quickly oxidized during the fast anodic potential scan, leading to a slight peak in the forward scan.

Our results have revealed one remarkable difference between Au and Pt NPs. The charge transfer coefficient α for Pt NPs was always greater than 0.5 but typically was smaller than 0.5 for Au NPs. The necessarily high α value on Pt results in the

DOI: 10.1021/acs.jpcc.5b11330
J. Phys. Chem. C 2016, 120, 20536–20546

Table 1. Averaged Values of the Different NP "Batches" for the Charge Transfer Coefficient (α) Determined from Simulation and Experimental Tafel Plots, the Standard Heterogeneous Electron Transfer Rate Constant (k^o), the Exchange Current Density (j_o), and the Gibbs Free Energy of Activation ($\Delta G^{\ddagger}_{NP}$)[a]

	α (simulation)	k^o (cm/s)	α (Tafel plot)	j_o (A/m^2)	$\Delta G^{\ddagger}_{NP}$ (kJ/mol)
5 nm Au	0.540 ± 0.020	8.75 ± 3.7 (10^{-5})	0.545 ± 0.016	3.00 ± 0.84	48.0 ± 1.1
12 nm Au	0.477 ± 0.015	9.64 ± 5.5 (10^{-6})	0.489 ± 0.015	11.5 ± 2.3	53.8 ± 1.0
50 nm Au	0.501 ± 0.015	7.08 ± 4.2 (10^{-6})	0.509 ± 0.017	26.5 ± 8.5	54.9 ± 1.0
4 nm Pt	0.742 ± 0.006	8.71 ± 2.0 (10^{-2})	0.777 ± 0.004	4750 ± 640	29.5 ± 0.4
10 nm Pt[b]	0.775 ± 0.003	7.66 ± 0.88 (10^{-2})	0.807 ± 0.004	4180 ± 590	29.6 ± 0.3
30 nm Pt	0.758 ± 0.007	4.23 ± 0.62 (10^{-2})	0.783 ± 0.007	1950 ± 270	31.1 ± 0.4

[a]All the values are determined from the same events which are simulated and are listed with the standard error of the mean. [b]Cubic NPs capped with polyacrylate.

simulated CVs having a smaller current response with a given potential change akin to the experimental curves. This was also observed for the CVs collected on Pt nanoelectrodes, which when simulated, had similar values for α and k^o and can be seen in Figure S9. The large α value means that for the Pt NPs there is a smaller current increase with increasing potential than for Au resulting in a somewhat elongated CV response, despite Pt's superior catalytic activity. This possibly indicates a competing surface reaction/species, such as adsorption of oxygen or protons, which is described in more details in the following paragraphs. The results in Figure 6 also show that k^o for Au is several orders of magnitude smaller than Pt.

A summary of α and k^o can be seen in Table 1. It is clear that the k^o increases as the particle size decreases, indicating an apparent increase in the activity as the radius decreases. This trend is observed for both Au and Pt, where all NPs have larger k^o than their corresponding bulk values. The increased catalytic activity of the smallest NPs is supported by Rotating Disk Electrode (RDE) experiments, shown in Figure S10, where the smallest NPs displayed the highest kinetic current densities.

Also listed in Table 1 is the averaged α determined from Tafel plots derived from the experimental CVs for the same set of events that were simulated. Values for α were calculated from the slope of the line in the Tafel plots and when compared to that obtained from the simulations there is a good match between the two. The exchange current density (j_o) determined from the Tafel plots was several orders of magnitude larger on the platinum NPs than on the gold NPs. The large exchange current density is likely due to the adsorption/desorption of protons from the solution. Even though these experiments were performed in 50 mM phosphate buffer at pH 7.4, there is still a response from the adsorption/desorption of hydrogen on Pt, which was unexpected (Figure S12). The regions of hydrogen desorption on the positive scan of a Pt UME overlaps with the hydrazine oxidation.

The hydrogen ions can block catalytic surface sites on the Pt and compete with the hydrazine molecules, shifting the oxidation to more positive potentials and causing the elongated CV response. This effect has been observed previously where the hydrazine oxidation potential on platinum UMEs is shifted positively in acidic solutions compared to basic solutions and the oxidation wave does not begin until after the proton desorption potential region in highly acidic solutions.[66] Alternatively, this effect could be due to a direct inhibition of the hydrazine oxidation due to the release of protons from the reaction. Proton adsorption has also been observed to interfere with the electrocatalytic reduction of oxygen on platinum, where the oxygen reduction current decreases as protons begin to adsorb on platinum.[71] The effect is much more pronounced for the NPs and nanoelectrodes as compared to the UME because of the low concentration of hydrogen ions in solution (pH 7.4). We think this competition effect, along with the increased mass transfer effects, may substantially shift the hydrazine oxidation to more positive potentials relative to bulk platinum, as discussed previously. This effect is significantly reduced on gold NPs due to the weaker affinity for hydrogen ions leading to a substantially smaller potential shift.

Gibbs Free Energy of Activation at Single Nanoparticles. Further analysis of single NP CVs allows for the determination of the Gibbs free energy of activation $\Delta G^{\ddagger}$ for hydrazine oxidation on both Au and Pt NPs. $\Delta G^{\ddagger}$ of activation can be calculated from the standard rate constant based on transition-state theory.[72,73]

$$k^o = k_{el} Z_{het} \exp\left(\frac{-\Delta G^{\neq}}{RT}\right) \tag{9}$$

where k_{el} is the electronic transmission coefficient (typically taken as unity for adiabatic processes)[72,73] and Z_{het} is the heterogeneous collision frequency factor. The collision frequency factor is defined as[72−74]

$$Z_{het} = \left(\frac{k_b T}{2\pi\mu}\right)^{1/2} \tag{10}$$

where μ is the reduced mass of the molecule and the NP (assuming a very large mass for the NP, μ reduces to the mass of the reactant molecule, hydrazine = 5.32×10^{-26} kg), and k_b is the Boltzmann constant. The calculated $\Delta G^{\ddagger}_{NP}$ is positive and decreases with the particle size, meaning the energy barrier decreases with decreasing NP size. The Au NPs have larger $\Delta G^{\ddagger}_{NP}$ than the Pt, which is consistent with their higher overpotentials. There is a larger shift in the average $\Delta G^{\ddagger}_{NP}$ for the 5 nm gold particles compared to the 12 and 50 nm ones. All of the NP batches had calculated average values of $\Delta G^{\ddagger}_{NP}$ that were below the values for the bulk metals (58.38 kJ/mol for bulk Au and 42.31 kJ/mol for Pt). A comparison of $\Delta G^{\ddagger}_{NP}$ between Pt NPs also showed a decreasing trend as particles get smaller. However, the different Pt particles have very similar values for $\Delta G^{\ddagger}_{NP}$ and did not show the same trend as the gold NPs.

To further explain the trend seen in the gold NPs we calculated a predicted shift of the $\Delta G^{\ddagger}_{NP}$ based on a theoretical extrapolation where we assumed the NPs were spherical and the change in energy is due to size alone. The shift of $\Delta G^{\ddagger}_{NP}$ has been predicted previously and takes the form of the Gibbs−Thomson relation,[9,75−77]

DOI: 10.1021/acs.jpcc.5b11330
J. Phys. Chem. C 2016, 120, 20536−20546

$$\Delta G^{\ddagger}_{NP} = \Delta G^{\ddagger}_{B} \pm \Delta G_{r} = \Delta G^{\ddagger}_{B} \pm \frac{2v\sigma_{r}}{r} \quad (11)$$

where $\Delta G^{\ddagger}_{B}$ is the free energy of activation on the bulk electrode, ΔG_{r} is the size-dependent free energy of activation, v is the partial molar volume of the element (1.021×10^{-5} m^3/mol for gold and 9.1×10^{-6} m^3/mol for Pt),[75] and r is the NP radius. The change in Gibbs free energy can have either a positive or a negative effect on the activation barrier, depending on the nature of the reaction. In this case, the effect decreases the Gibbs free energy for the NP relative to the bulk, indicating a lowering of the energy barrier. The variable σ_r is the size (radius)-dependent surface energy of the particl, which has the following form,[38,78,79]

$$\sigma_{r} = \sigma_{B}\left(1 - \frac{1}{\left(\frac{2d}{h} - 1\right)}\right) \exp\left(-\frac{2S_{B}}{3R}\frac{1}{\left(\frac{2d}{h} - 1\right)}\right) \quad (12)$$

where σ_B is the surface tension of the bulk material (1880 erg/cm^2 or 1.88 J/m^2 for Au and 3240 erg/cm^2 or 3.24 J/m^2 for Pt),[75] d is the NP diameter, h is the atomic diameter (0.289 nm for Au and 0.277 nm for Pt),[80] S_B is the cohesive entropy of the material, which is equal to E_b/T_b. E_b is the bulk cohesive energy (3.81 eV or 367.6 kJ/mol for Au and 5.84 eV or 563.46 kJ/mol for Pt)[81] and T_b is the bulk solid vapor transition temperature (3129 K for Au and 4098 K for Pt).[82] The calculated curve for the value of $\Delta G^{\ddagger}_{NP}$ shows the largest deviation from bulk at approximately 1 nm radius and then is seen to increase very rapidly again. By plotting the theoretical size-dependent free energy curve (calculated with eqs 11 and 12) and plotting the measured $\Delta G^{\ddagger}_{NP}$ of the different sized NPs (calculated with eqs 9 and 10), we see that gold follows the theoretical curve, but platinum does not, as shown in Figure 7. The larger diameter gold NPs closely follow the calculated curve and the smaller diameter NPs are seen to decrease in activation energy, which is again, consistent with the calculated curve. The platinum NPs are seen to decrease in the value of $\Delta G^{\ddagger}_{NP}$ with decreasing size but do not fall closely in line with the calculated curve. The deviation of the platinum NPs from the prediction may be due to the structural and surface differences between the different-sized particles in addition to the hydrogen adsorption competition. On average, the Au NPs have very similar shapes, roughness, and ligands, whereas the Pt NPs vary between particles.

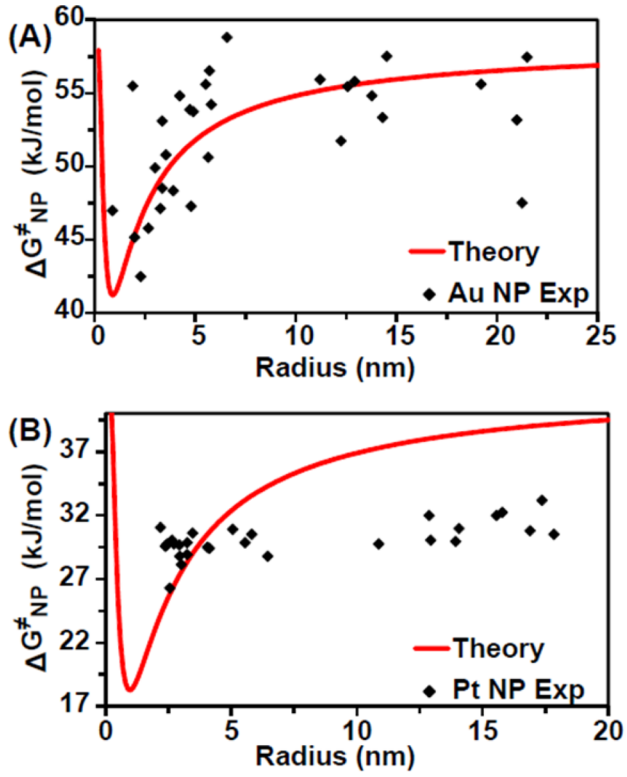

Figure 7. Average Gibbs free energy of activation plotted vs NP size for the individual gold (A) and platinum (B) NPs. Also shown in each plot is the theoretical prediction of the change in $\Delta G^{\ddagger}_{NP}$, as predicted from eq 11. The gold NPs are seen to follow the predictive curve more closely than the platinum NPs.

CONCLUSIONS

In summary, the use of FSCV has enabled us to investigate and better understand electrocatalytic activity of single platinum and gold NPs of different sizes, shapes, and capping ligands for hydrazine oxidation and how the data can be misinterpreted if mass transfer is not taken into account. Seemingly, the overpotential for hydrazine oxidation on single NPs appears to generally increase as particles gets smaller, largely attributed to increased mass transfer rates. If the mass transfer effect is not taken into account then one could deduce the nanoparticles were becoming less active as the size decreased. By simulating the experimental CVs, we have shown that key kinetic parameters, such as the standard electron-transfer rate constant and the charge transfer coefficient, can be determined and used to more correctly assess the catalytic activity. We have determined that the capping agent could play a more substantial role in the activity than the nature of the NP crystallinity and surface orientation. The Gibbs free energy of activation was also calculated from the electron transfer rate constant and was found to be smaller for the NPs than compared to bulk metals, indicating a lower energy barrier. The change in the Gibbs free energy with changing NP size follows a theoretical model well for gold, but less so for platinum. We believe the competition between hydrazine and adsorbed hydrogen ions for surface sites on the Pt surface, in part, explains the deviation of the Pt NPs from the theoretical prediction. Single NP analysis using FSCV combined with simulations can be a powerful tool in many aspects of future catalytic analysis.

ASSOCIATED CONTENT

Supporting Information

The Supporting Information is available free of charge on the ACS Publications website at DOI: 10.1021/acs.jpcc.5b11330.

The detailed experimental procedure including a list of used chemicals, statistical analysis, a table of the NP average measured sizes with standard distributions and number of particles measured, a table with the constants and variables used in the simulations, a table listing the number of total collisions, number that reached steady state and number simulated for each nanoparticle batch, voltammetric response of a carbon fiber electrodes before and after exposure, TEM images and histograms of the measured NPs sizes, E_{onset} and $E_{1/2}$ histograms, schematic of the simulation environment including a screen shot of the simulated concentration profile, NP simulations showing the effect of changing the value of α or k^o,

DOI: 10.1021/acs.jpcc.5b11330
J. Phys. Chem. C 2016, 120, 20536−20546

simulated NP CVs using the same α and k^o parameters showing the effect of NP size on overpotential, Tafel plots made from the examples CVs in Figure 6, plot of platinum nanoelectrode shifting hydrazine $E_{1/2}$ with electrode radius, and plots of a Pt UME in 50 mM phosphate buffer with normalized hydrogen ion desorption peaks and normalized NP hydrazine CV, simulated hydrazine oxidation CVs from two example platinum disk nanoelectrodes, rotating disk electrode CVs and Levich plots with discussion (PDF).

AUTHOR INFORMATION

Corresponding Author

*Phone: (206) 543-1767. E-mail: zhang@chem.washington.edu.

Notes

The authors declare no competing financial interest.

ACKNOWLEDGMENTS

The authors gratefully acknowledge financial support by the Defense Threat Reduction Agency (HDTRA1-11-1-0005) and AFOSR MURI (FA9550-14-1-0003). Part of this work was conducted at the University of Washington NanoTech User Facility, a member of the National Science Foundation, National Nanotechnology Infrastructure Network (NNIN). We also thank Professor R. Mark Wightman at University of North Carolina for allowing us to use the HDCV program.

REFERENCES

(1) Fan, F.-R. F.; Bard, A. J. Electrochemical Detection of Single Molecules. *Science* **1995**, *267*, 871−874.

(2) Sun, P.; Mirkin, M. V. Electrochemistry of Individual Molecules in Zeptoliter Volumes. *J. Am. Chem. Soc.* **2008**, *130*, 8241−8250.

(3) Zevenbergen, M. A. G.; Singh, P. S.; Goluch, E. D.; Wolfrum, B. L.; Lemay, S. G. Stochastic Sensing of Single Molecules in a Nanofluidic Electrochemical Device. *Nano Lett.* **2011**, *11*, 2881−2886.

(4) Rosi, N. L.; Giljohann, D. A.; Thaxton, C. S.; Lytton-Jean, A. K. R.; Han, M. S.; Mirkin, C. A. Oligonucleotide-Modified Gold Nanoparticles for Intracellular Gene Regulation. *Science* **2006**, *312*, 1027−1030.

(5) Peng, G.; Tisch, U.; Adams, O.; Hakim, M.; Shehada, N.; Broza, Y. Y.; Billan, S.; Abdah-Bortnyak, R.; Kuten, A.; Haick, H. Diagnosing Lung Cancer in Exhaled Breath Using Gold Nanoparticles. *Nat. Nanotechnol.* **2009**, *4*, 669−673.

(6) Han, X.; Liu, Y.; Yin, Y. Colorimetric Stress Memory Sensor Based on Disassembly of Gold Nanoparticle Chains. *Nano Lett.* **2014**, *14*, 2466−2470.

(7) Cheng, Y.; Stakenborg, T.; Van Dorpe, P.; Lagae, L.; Wang, M.; Chen, H.; Borghs, G. Fluorescence Near Gold Nanoparticles for DNA Sensing. *Anal. Chem.* **2011**, *83*, 1307−1314.

(8) Cui, C.; Gan, L.; Heggen, M.; Rudi, S.; Strasser, P. Compositional Segregation in Shaped Pt Alloy Nanoparticles and Their Structural Behaviour During Electrocatalysis. *Nat. Mater.* **2013**, *12*, 765−771.

(9) Campbell, C. T.; Parker, S. C.; Starr, D. E. The Effect of Size-Dependent Nanoparticle Energetics on Catalyst Sintering. *Science* **2002**, *298*, 811−814.

(10) Crespo-Quesada, M.; Yarulin, A.; Jin, M.; Xia, Y.; Kiwi-Minsker, L. Structure Sensitivity of Alkynol Hydrogenation on Shape- and Size-Controlled Palladium Nanocrystals: Which Sites Are Most Active and Selective. *J. Am. Chem. Soc.* **2011**, *133*, 12787−12794.

(11) Hamilton, J. F.; Baetzold, R. C. Catalysis by Small Metal Clusters. *Science* **1979**, *205*, 1213−1220.

(12) Ye, H.; Crooks, J. A.; Crooks, R. M. Effect of Particle Size on the Kinetics of the Electrocatalytic Oxygen Reduction Reaction Catalyzed by Pt Dendrimer-Encapsulated Nanoparticles. *Langmuir* **2007**, *23*, 11901−11906.

(13) Campbell, C. T. The Energetics of Supported Metal Nanoparticles: Relationships to Sintering Rates and Catalytic Activity. *Acc. Chem. Res.* **2013**, *46*, 1712−1719.

(14) Burda, C.; Chen, X.; Narayanan, R.; El-Sayed, M. A. Chemistry and Properties of Nanocrystals of Different Shapes. *Chem. Rev.* **2005**, *105*, 1025−1102.

(15) Bratlie, K. M.; Lee, H.; Komvopoulos, K.; Yang, P.; Somorjai, G. A. Platinum Nanoparticle Shape Effects on Benzene Hydrogenation Selectivity. *Nano Lett.* **2007**, *7*, 3097−3101.

(16) Kwon, S. G.; Krylova, G.; Sumer, A.; Schwartz, M. M.; Bunel, E. E.; Marshall, C. L.; Chattopadhyay, S.; Lee, B.; Jellinek, J.; Shevchenko, E. V. Capping Ligands as Selectivity Switchers in Hydrogenation Reactions. *Nano Lett.* **2012**, *12*, 5382−5388.

(17) Chen, G.; Zhao, Y.; Fu, G.; Duchesne, P. N.; Gu, L.; Zheng, Y.; Weng, X.; Chen, M.; Zhang, P.; Pao, C. W.; et al. Interfacial Effects in Iron-Nickel Hydroxide-Platinum Nanoparticles Enhance Catalytic Oxidation. *Science* **2014**, *344*, 495−499.

(18) Quinn, B. M.; van't Hof, P. G.; Lemay, S. G. Time-Resolved Electrochemical Detection of Discrete Adsorption Events. *J. Am. Chem. Soc.* **2004**, *126*, 8360−8361.

(19) Fosdick, S. E.; Anderson, M. J.; Nettleton, E. G.; Crooks, R. M. Correlated Electrochemical and Optical Tracking of Discrete Collision Events. *J. Am. Chem. Soc.* **2013**, *135*, 5994−5997.

(20) Dick, J. E.; Hilterbrand, A. T.; Boika, A.; Upton, J. W.; Bard, A. J. Electrochemical Detection of a Single Cytomegalovirus at an Ultramicroelectrode and its Antibody Anchoring. *Proc. Natl. Acad. Sci. U. S. A.* **2015**, *112*, 5303−5308.

(21) Kim, B.-K.; Kim, J.; Bard, A. J. Electrochemistry of a Single Attoliter Emulsion Droplet in Collisions. *J. Am. Chem. Soc.* **2015**, *137*, 2343−2349.

(22) Xiao, X.; Bard, A. J. Observing Single Nanoparticle Collisions at an Ultramicroelectrode by Electrocatalytic Amplification. *J. Am. Chem. Soc.* **2007**, *129*, 9610−9612.

(23) Xiao, X.; Fan, F.-R. F.; Zhou, J.; Bard, A. J. Current Transients in Single Nanoparticle Collision Events. *J. Am. Chem. Soc.* **2008**, *130*, 16669−16677.

(24) Zhou, H.; Park, J. H.; Fan, F.-R. F.; Bard, A. J. Observation of Single Metal Nanoparticle Collisions by Open Circuit (Mixed) Potential Changes at an Ultramicroelectrode. *J. Am. Chem. Soc.* **2012**, *134*, 13212−13215.

(25) Kleijn, S. E. F.; Lai, S. C. S.; Miller, T. S.; Yanson, A. I.; Koper, M. T. M.; Unwin, P. R. Landing and Catalytic Characterization of Individual Nanoparticles on Electrode Surfaces. *J. Am. Chem. Soc.* **2012**, *134*, 18558−18561.

(26) Dasari, R.; Tai, K.; Robinson, D. A.; Stevenson, K. J. Electrochemical Monitoring of Single Nanoparticle Collisions at Mercury-Modified Platinum Ultramicroelectrodes. *ACS Nano* **2014**, *8*, 4539−4546.

(27) Kang, M.; Perry, D.; Kim, Y.-R.; Colburn, A. W.; Lazenby, R. A.; Unwin, P. R. Time-Resolved Detection and Analysis of Single Nanoparticle Electrocatalytic Impacts. *J. Am. Chem. Soc.* **2015**, *137*, 10902−10905.

(28) Alligrant, T. M.; Anderson, M. J.; Dasari, R.; Stevenson, K. J.; Crooks, R. M. Single Nanoparticle Collisions at Microfluidic Microband Electrodes: The Effect of Electrode Material and Mass Transfer. *Langmuir* **2014**, *30*, 13462−13469.

(29) Jung, A. R.; Lee, S.; Joo, J. W.; Shin, C.; Bae, H.; Moon, S. G.; Kwon, S. J. Potential-Controlled Current Responses from Staircase to Blip in Single Pt Nanoparticle Collisions on a Ni Ultramicroelectrode. *J. Am. Chem. Soc.* **2015**, *137*, 1762−1765.

(30) Fernando, A.; Parajuli, S.; Alpuche-Aviles, M. A. Observation of Individual Semiconducting Nanoparticle Collisions by Stochastic Photoelectrochemical Currents. *J. Am. Chem. Soc.* **2013**, *135*, 10894−10897.

(31) Sekretaryova, A. N.; Vagin, M. Yu; Turner, A. P. F.; Eriksson, M. Electrocatalytic Currents from Single Enzyme Molecules. *J. Am. Chem. Soc.* **2016**, *138*, 2504−2507.

DOI: 10.1021/acs.jpcc.5b11330
J. Phys. Chem. C 2016, 120, 20536−20546

(32) Hao, R.; Fan, Y. S.; Zhang, B. Electrocatalytic Reduction of Silver Chloride on Single Metal Nanoparticles. *J. Electrochem. Soc.* **2016**, *163*, H3145−H3151.
(33) Zhou, Y.-G.; Rees, N. V.; Compton, R. G. The Electrochemical Detection and Characterization of Silver Nanoparticles in Aqueous Solution. *Angew. Chem., Int. Ed.* **2011**, *50*, 4219−4221.
(34) Stuart, E. J. E.; Tschulik, K.; Batchelor-McAuley, C.; Compton, R. G. Electrochemical Observation of Single Collision Events: Fullerene Nanoparticles. *ACS Nano* **2014**, *8*, 7648−7654.
(35) Perera, N.; Karunathilake, N.; Chhetri, P.; Alpuche-Aviles, M. A. Electrochemical Detection and Sizing of Colloidal ZnO Nanoparticles. *Anal. Chem.* **2015**, *87*, 777−784.
(36) Dunevall, J.; Fathali, H.; Najafinobar, N.; Lovric, J.; Wigström, J.; Cans, A.-S.; Ewing, A. G. Characterizing the Catecholamine Content of Single Mammalian Vesicles by Collision−Adsorption Events at an Electrode. *J. Am. Chem. Soc.* **2015**, *137*, 4344−4346.
(37) Shan, X.; Díez-Pérez, I.; Wang, L.; Wiktor, P.; Gu, Y.; Zhang, L.; Wang, W.; Lu, J.; Wang, S.; Gong, Q.; et al. Imaging the Electrocatalytic Activity of Single Nanoparticles. *Nat. Nanotechnol.* **2012**, *7*, 668−672.
(38) Zhou, X.; Xu, W.; Liu, G.; Panda, D.; Chen, P. Size-Dependent Catalytic Activity and Dynamics of Gold Nanoparticles at the Single-Molecule Level. *J. Am. Chem. Soc.* **2010**, *132*, 138−146.
(39) Zhou, X.; Andoy, N. M.; Liu, G.; Choudhary, E.; Han, K.-S.; Shen, H.; Chen, P. Quantitative Super-Resolution Imaging Uncovers Reactivity Patterns on Single Nanocatalysts. *Nat. Nanotechnol.* **2012**, *7*, 237−241.
(40) Li, Y.; Cox, J. T.; Zhang, B. Electrochemical Responses and Electrocatalysis at Single Au Nanoparticles. *J. Am. Chem. Soc.* **2010**, *132*, 3047−3054.
(41) Kim, J.; Kim, B.-K.; Cho, S. K.; Bard, A. J. Tunneling Ultramicroelectrode Nanoelectrodes and Nanoparticle Collisions. *J. Am. Chem. Soc.* **2014**, *136*, 8173−8176.
(42) Chen, S.; Kucernak, A. Electrocatalysis under Conditions of High Mass Transport Rate: Oxygen Reduction on Single Submicrometer-Sized Pt Particles Supported on Carbon. *J. Phys. Chem. B* **2004**, *108*, 3262−3276.
(43) Sun, P.; Li, F.; Yang, C.; Sun, T.; Kady, I.; Hunt, B.; Zhuang, J. Formation of a Single Gold Nanoparticle on a Nanometer-Sized Electrode and Its Electrochemical Behaviors. *J. Phys. Chem. C* **2013**, *117*, 6120−6125.
(44) Tel-Vered, R.; Bard, A. J. Generation and Detection of Single Metal Nanoparticles Using Scanning Electrochemical Microscopy Techniques. *J. Phys. Chem. B* **2006**, *110*, 25279−25287.
(45) Armstrong-James, M.; Millar, J.; Kruk, Z. L. Quantification of Noradrenaline Iontophoresis. *Nature* **1980**, *288*, 181−183.
(46) Baur, J. E.; Kristensen, E. W.; May, L. J.; Wiedemann, D. J.; Wightman, R. M. Fast-Scan Voltammetry of Biogenic Amines. *Anal. Chem.* **1988**, *60*, 1268−1272.
(47) Heien, M. L. A. V.; Johnson, M. A.; Wightman, R. M. Resolving Neurotransmitters Detected by Fast-Scan Cyclic Voltammetry. *Anal. Chem.* **2004**, *76*, 5697−5704.
(48) Guo, Z.; Percival, S. J.; Zhang, B. Chemically Resolved Transient Collision Events of Single Electrocatalytic Nanoparticles. *J. Am. Chem. Soc.* **2014**, *136*, 8879−8882.
(49) Rosca, V.; Duca, M.; de Groot, M. T.; Koper, M. T. M. Nitrogen Cycle Electrocatalysis. *Chem. Rev.* **2009**, *109*, 2209−2244.
(50) Sanabria-Chinchilla, J.; Asazawa, K.; Sakamoto, T.; Yamada, K.; Tanaka, H.; Strasser, P. Noble Metal-Free Hydrazine Fuel Cell Catalysts: EPOC Effect in Competing Chemical and Electrochemical Reaction Pathways. *J. Am. Chem. Soc.* **2011**, *133*, 5425−5431.
(51) Kleijn, S. E. F.; Serrano-Bou, B.; Yanson, A. I.; Koper, M. T. M. Influence of the Hydrazine-Induced Aggregation on the Electrochemical Detection of Platinum Nanoparticles. *Langmuir* **2013**, *29*, 2054−2064.
(52) Bucher, E. S.; Brooks, K.; Verber, M.; Keithley, R. B.; Owesson-White, C.; Carroll, S.; Takmakov, P.; McKinney, C. J.; Wightman, R. M. Flexible Software Platform for Fast-Scan Cyclic Voltammetry Data Acquisition and Analysis. *Anal. Chem.* **2013**, *85*, 10344−10353.
(53) Karp, S.; Meites, L. The Voltammetric Characteristics and Mechanism of Electrooxidation of Hydrazine. *J. Am. Chem. Soc.* **1962**, *18*, 906−912.
(54) PEM *Fuel Cell Electrocatalysts and Catalyst Layers: Fundamentals and Applications*; Zhang, J., Ed.; Springer-Verlag: London, 2008.
(55) Zhang, J.; Sasaki, K.; Sutter, E.; Adzic, R. R. Stabilization of Platinum Oxygen-Reduction Electrocatalysts Using Gold Clusters. *Science* **2007**, *315*, 220−222.
(56) Mistry, H.; Reske, R.; Zeng, Z.; Zhao, Z.-J.; Greeley, J.; Strasser, P.; Cuenya, B. R. Exceptional Size-Dependent Activity Enhancement in the Electroreduction of CO_2 over Au Nanoparticles. *J. Am. Chem. Soc.* **2014**, *136*, 16473−16476.
(57) Li, Y.; Bergman, D.; Zhang, B. Preparation and Electrochemical Response of 1−3 nm Pt Disk Electrodes. *Anal. Chem.* **2009**, *81*, 5496−5502.
(58) Watkins, J. J.; Chen, J.; White, H. S.; Abruña, H. D.; Maisonhaute, E.; Amatore, C. Zeptomole Voltammetric Detection and Electron-Transfer Rate Measurements Using Platinum Electrodes of Nanometer Dimensions. *Anal. Chem.* **2003**, *75*, 3962−3971.
(59) Mirkin, M. V.; Bard, A. J. Simple Analysis of Quasi-Reversible Steady-State Voltammograms. *Anal. Chem.* **1992**, *64*, 2293−2302.
(60) Watanabe, M.; Sei, H.; Stonehart, P. The Influence of Platinum Crystallite Size on the Electroreduction of Oxygen. *J. Electroanal. Chem. Interfacial Electrochem.* **1989**, *261*, 375−387.
(61) Hayden, B. E. Particle Size and Support Effects in Electrocatalysis. *Acc. Chem. Res.* **2013**, *46*, 1858−1866.
(62) Tsunoyama, H.; Ichikuni, N.; Sakurai, H.; Tsukuda, T. Effect of Electronic Structures of Au Clusters Stabilized by Poly(*N*-vinyl-2-pyrrolidone) on Aerobic Oxidation Catalysis. *J. Am. Chem. Soc.* **2009**, *131*, 7086−7093.
(63) Rosca, V.; Koper, M. T. M. Electrocatalytic Oxidation of Hydrazine on Platinum Electrodes in Alkaline Solutions. *Electrochim. Acta* **2008**, *53*, 5199−5205.
(64) Briskeby, S. T.; Tsypkin, M.; Tunold, R.; Sunde, S. Preparation of Electrocatalysts by Reduction of Precursers with Sodium Citrate. *RSC Adv.* **2014**, *4*, 44185−44192.
(65) Chen, C.-H.; Jacobse, L.; McKelvey, K.; Lai, S. C. S.; Koper, M. T. M.; Unwin, P. R. Voltammetric Scanning Electrochemical Cell Microscopy: Dynamic Imaging of Hydrazine Electro-oxidation on Platinum Electrodes. *Anal. Chem.* **2015**, *87*, 5782−5789.
(66) Aldous, L.; Compton, R. G. The Mechanism of Hydrazine Electro-oxidation Revealed by Platinum Microelectrodes: Role of Residual Oxides. *Phys. Chem. Chem. Phys.* **2011**, *13*, 5279−5287.
(67) Percival, S. J.; Zhang, B. Study of the Formation and Quick Growth of Thick Oxide Films Using Platinum Nanoelectrodes as a Model Electrocatalyst. *Langmuir* **2014**, *30*, 11235−11242.
(68) Li, J.; Xie, H.; Chen, L. A Sensitive Hydrazine Electrochemical Sensor Based on Electrodeposition of Gold Nanoparticles on Choline Film Modified Glassy Carbon Electrode. *Sens. Actuators, B* **2011**, *153*, 239−245.
(69) Scharf, U.; Grabner, E. Electrocatalytic Oxidation of Hydrazine at a Prussian Blue-Modified Glassy Carbon Electrode. *Electrochim. Acta* **1996**, *41*, 233−239.
(70) Bard, A. J.; Faulkner, L. R. *Elecrochemical Methods*, 2nd ed.; John Wiley & Sons: New York, 2001.
(71) Percival, S. J.; Zhang, B. Electrocatalytic Reduction of Oxygen at Single Platinum Nanowires. *J. Phys. Chem. C* **2013**, *117*, 13928−13935.
(72) Marcus, R. A. On the Theory of Electron Transfer Reactions. VI. Unified Treatment for Homogeneous and Electrode Reactions. *J. Chem. Phys.* **1965**, *43*, 679−701.
(73) Hupp, J. T.; Weaver, M. J. The Frequency Factor for Outer-Sphere Electrochemical Reactions. *J. Electroanal. Chem. Interfacial Electrochem.* **1983**, *152*, 1−14.
(74) Jung, L. S.; Campbell, C. T. Sticking Probabilities in Adsorption of Alkanethiols from Liquid Ethanol Solution onto Gold. *J. Phys. Chem. B* **2000**, *104*, 11168−11178.
(75) Plieth, W. J. Electrochemical Properties of Small Clusters of Metal Atoms and Their Role in Surface Enhanced Raman Scattering. *J. Phys. Chem.* **1982**, *86*, 3166−3170.

DOI: 10.1021/acs.jpcc.5b11330
J. Phys. Chem. C 2016, 120, 20536−20546

(76) Parmon, V. N. Thermodynamic Analysis of the Effect of the Nanoparticle Size of the Active Component on the Adsorption Equilibrium and the Rate of Heterogeneous Catalytic Processes. *Dokl. Phys. Chem.* **2007**, *413*, 42−48.
(77) Murzin, D. Y. Thermodynamic Analysis of Nanoparticle Size Effect on Catalytic Kinetics. *Chem. Eng. Sci.* **2009**, *64*, 1046−1052.
(78) Lu, H. M.; Jiang, Q. Size-Dependent Surface Energies of Nanocrystals. *J. Phys. Chem. B* **2004**, *108*, 5617−5619.
(79) Yang, C. C.; Li, S. Investigation of Cohesive Energy Effects on Size-Dependent Physical and Chemical Properties of Nanocrystals. *Phys. Rev. B: Condens. Matter Mater. Phys.* **2007**, *75*, 165413.
(80) Pauling, L. Atomic Radii and Interatomic Distances in Metals. *J. Am. Chem. Soc.* **1947**, *69*, 542−553.
(81) Elsässer, C.; Takeuchi, N.; Ho, K. M.; Chan, C. T.; Braun, P.; Fähnle, M. Relativistic Effects on Ground State Properties of 4d and 5d Transition Metals. *J. Phys.: Condens. Matter* **1990**, *2*, 4371−4394.
(82) CRC *Handbook of Chemistry and Physics*, 86th ed.; Lide, D. R., Ed.; CRC Press: Boca Raton, FL, 2005.

DOI: 10.1021/acs.jpcc.5b11330
J. Phys. Chem. C 2016, 120, 20536−20546